Biophysical Journal Volume 109 October 2015 1454–1462

Article

Uniform Contraction-Expansion Description of Relative Centromere and Telomere Motion

Eldad Kepten,[1,*] Aleksander Weron,[2] Irena Bronstein,[1] Krzysztof Burnecki,[2] and Yuval Garini[1,*]
[1]Physics Department & Institute of Nanotechnology, Bar Ilan University, Ramat Gan, Israel; and [2]Hugo Steinhaus Center, Department of Mathematics, Wroclaw University of Technology, Wroclaw, Poland

ABSTRACT Internal organization and dynamics of the eukaryotic nucleus have been at the front of biophysical research in recent years. It is believed that both dynamics and location of chromatin segments are crucial for genetic regulation. Here we study the relative motion between centromeres and telomeres at various distances and at times relevant for genetic activity. Using live-imaging fluorescent microscopy coupled to stochastic analysis of relative trajectories, we find that the interlocus motion is distance-dependent with a varying fractional memory. In addition to short-range constraining, we also observe long-range anisotropic-enhanced parallel diffusion, which contradicts the expectation for classic viscoelastic systems. This motion is linked to uniform expansion and contraction of chromatin in the nucleus, and leads us to define and measure a new (to our knowledge) uniform contraction-expansion diffusion coefficient that enriches the contemporary picture of nuclear behavior. Finally, differences between loci types suggest that different sites along the genome experience distinctive coupling to the nucleoplasm environment at all scales.

INTRODUCTION

In eukaryotic cells, the genetic activity is localized to the nucleus where genes are encoded in long DNA strands named chromosomes (1) that are packed by nucleosomes to create the chromatin fibers (2). The transcription of genes into RNA in the nucleus and later translation of RNA into proteins in the cytoplasm is regulated through several layers of control mechanisms. The dynamical organization of chromatin forms a central part of the regulatory pathways through cross influences between chromatin segments (3) and spatial packaging (4). Studies have shown that chromatin organization is far from an equilibrium polymer melt (5). Each chromosome occupies a separate volume termed a "chromosome territory" and a complex spatial organization appears inside each territory (6,7).

The dynamics of tracer particles and their stochastic characteristics hold crucial information regarding the underlying biological mechanisms (8) and the surrounding media (9). Previous studies (10–15) have shown that the typical motion of a chromatin locus is localized, stemming from anomalous subdiffusion, i.e., $\langle x^2 \rangle \sim Dt^{\alpha}$ with $\alpha < 1$ (16). Dynamics obey the characteristics of a fractional Brownian motion (FBM), as expected for a monomer in a viscoelastic media (17) and qualitatively reproduced in simulations (18,19). In addition, it is hypothesized that genetic activity can bring about further motion bursts (20). A recent study in live cells has shown that the rapid motion of chromatin over several seconds is positively correlated across micron-scale distances and neighboring chromosomes territories (21).

The dynamic interactions between chromosome loci in different chromosome territories, and the stochastic characteristics of this interaction, are far from understood. This is especially true when looking at timescales relevant to genetic activity and control (several minutes). However, this information is crucial to understand and model nuclear activity.

Our objective is to study the relative dynamics between chromatin loci to characterize nuclear dynamics at such timescales. To this end, we measured the relative dynamics between thousands of telomere (chromosome ends) and centromere (toward the chromosome center) pairs in dozens of cells, at timescales of minutes. As we show, telomeres and centromeres are distributed rather homogeneously in the nucleus, presenting a picture of the general interchromosomal motion of nuclear chromatin.

Telomeres and centromeres may experience different constraints on their motion. Telomeres are located at the ends of the chromosomes, and are perhaps less restricted by the polymeric structure than centromeres that are located more toward the center. In addition, telomeres and centromeres experience different protein interactions and perform different nuclear roles. By taking two different loci types, we can identify variations in the dynamics between these genetic sites in addition to common mechanisms that may be relevant to other chromatin foci.

In what follows, we show that the stochastic model describing the motions changes with distance and locus type. At short interpair distances the relative motion is

Submitted February 23, 2015, and accepted for publication July 20, 2015.

*Correspondence: eldad.kepten@biu.ac.il or yuval.garini@biu.ac.il

Editor: Paul Wiseman.

0006-3495/15/10/1454/9

http://dx.doi.org/10.1016/j.bpj.2015.07.031

constrained and hindered. Surprisingly, at distances of a few microns a significant anisotropy is seen, unpredicted by past works and contradicting equilibrium soft-matter models. Stochastic analysis shows that relative motion has a strong fractional memory, albeit distance-dependent and anisotropic. We propose that the anisotropy and fractional nature can be explained through continuous uniform expansion and contraction of the nucleus. The measurement and analysis schemes, and the suggested model, are all validated through simulations. Our analysis technique enables the measurement of this coefficient far below the optical diffraction limit.

MATERIALS AND METHODS

Cell culture

Human U2OS osteosarcoma cells were grown and transfected according to an established procedure (15). For loci tracking experiments, telomeres were tagged with a GFP-TRF2 plasmid, which is known to localize on shelterin complex around the telomeres. Centromeres were tagged with CENPA-eGFP that localizes on the centromere. These fluorescent complexes are believed to have no preference between chromosomes. The variations in fluorescent intensity arise from variations in genetic site sizes and random binding dynamics at each site.

To label the nuclear envelope, we transfected cells with plasmids coding for eGFP-pre-laminA. Lamins are a central part of the nuclear lamina and are a common marker for its location. These cells were also transfected with a TRF1-RFP plasmid to tag telomeres. In this set of measurements, a red color was chosen for telomeres to improve contrast in respect to the eGFP-pre-laminA.

Fluorescent microscopy and image analysis

Cells were measured with a model No. FV-1000 confocal microscope (Olympus, Melville, NY), with a 60× oil lens of NA 1.42. Cells were maintained in a miniature incubator regulated at 37°C and 5% CO_2. We searched for elliptically shaped nuclei presenting high fluorescence of intact telomere and centromere structures with minimal background signal. For each adequate nucleus, 35 z sections at intervals of 0.35 μm, and an encompassing XY plane at 0.1 μm per pixel, were set. One-hundred time points were measured at free run settings, with a time step of 18.5 s. Thus, we measure trajectories of 1850 s, i.e., 31 min. Image series were checked for drift out of focal plane, or the appearance of nuclear shape abnormalities. A typical cell is shown in Fig. 1 *A*.

Adding our new measurements to our previous database (17), we have >1100 telomere and 500 centromere trajectories, giving 10,400 and 6000 pairs, respectively. We estimate that ~95% of pairs are from different chromosome chains (as there are only two telomeres and one centromere per chromosome).

Image series were analyzed with the commercial IMARIS software (IMARIS BITPLANE, http://www.bitplane.com/imaris/imaris) that identifies spot centers and connects them into trajectories. We performed a visual inspection of each extracted trajectory, demanding that it does not cross other trajectories, that no jumping between particles is seen and that no time points are missing. After the coordinates of all trajectories in each cell were extracted, the center of mass of the nucleus was calculated and subtracted to correct for cell drift. Rotation was corrected by calculating the average rotation matrix of loci around the center of mass.

Trajectory data analysis

Measurement of formaldehyde-fixed cells enabled us to extract the measurement error in our system. We found a one-dimensional localization error standard deviation of $\sigma_N = 16$ nm in the XY plane, and 90 nm in the z axis. This is due to shot noise and the limiting effect of the point-spread function inherent to optical microscopy.

Because we have 100 time points, the increased error in the z axis is averaged out when calculating the average distance between loci pairs. This is because, when measuring distances, errors are averaged with their sign, quickly canceling each other and converging to the true average value. Thus, we can accurately extract the three-dimensional distance between pairs. However, when calculating the mean-square difference (MSD) and other statistical characteristics, the z errors do not cancel out and are not negligible. This arises from the fact that in MSDs, the errors appear squared, and thus contribute only a positive offset (22).

Thus we analyzed the relative motion only in the two-dimensional XY plane (i.e., to eliminate the increased error in z). That said, recalculating relative dynamics in U2OS cells, using only telomere pairs on the same focal plane, gave similar results (with increased noise due to the significant decrease in the amount of analyzed relative trajectories).

For two moving particles in two dimensions, it is beneficial to study their relative dynamics in the components parallel and perpendicular to their connecting vector (Fig. 1, *inset*). Specifically, take two particles at locations $r_1(t)$ and $r_2(t)$, which move $\delta r_1(t)$ and $\delta r_2(t)$ at time point t. We first calculate the normalized vector $e_{12}^{\parallel}(t)$ pointing from $r_1(t)$ to $r_2(t)$ at each time point. Then, the component $\delta r_1^{\parallel}(t) = \delta r_1(t) \cdot e_{12}^{\parallel}(t)$ is the parallel step of the first

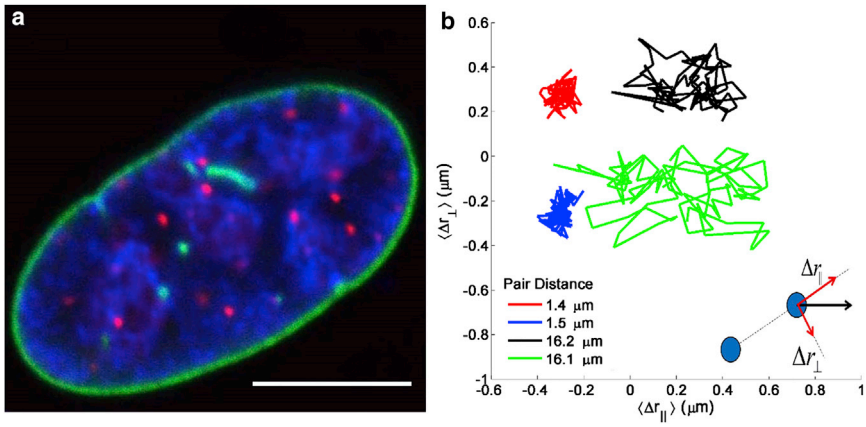

FIGURE 1 (*a*) Typical U2OS cell cross section. Telomeres are tagged with TRF1-RFP (*red*). (*Green*) eGFP-pre-laminA proteins, which are mainly concentrated on the nuclear envelope. General chromatin (*blue*) shown by Hoechst staining. Note the random distribution of telomeres and the ellipsoidal shape of the nucleus. Scale bar = 10 μm. (*b*) Relative diffusion of representative trajectories of four centromere pairs presented in orthogonal motion components. Two pairs are at close distances of $\bar{r} \approx 1.5$ μm (*left*, *red* and *blue*) and two pairs are at a distance of $\bar{r} \approx 16$ μm (*right*, *black* and *green*). The distant pairs have much higher relative motion, while the close pairs show highly constrained motion. In the distant pairs, it appears that the parallel motion is more significant. Each pair is from a different cell. (*Inset*) The relative step between two particles (*black*) is decomposed into a parallel, $\Delta r_{||}$, and perpendicular, $\Delta r_{\perp}$ step (*red*). To see this figure in color, go online.

particle in respect to the second particle at time point t. Using the orthonormal vector $e_{12}^{\perp}(t)$ in the two-dimensional plane, the perpendicular component can also be calculated. The same is done for the second particle.

Next, one calculates the parallel relative trajectory $r_{12}^{\parallel} = \sum_t(\delta r_1^{\parallel}(t) - \delta r_2^{\parallel}(t))$ and the perpendicular trajectory $r_{12}^{\perp} = \sum_t(\delta r_1^{\perp}(t) - \delta r_2^{\perp}(t))$. These two components of the relative motion can be simplistically attributed to expansions and contractions for the parallel motion and rotational dynamics for the perpendicular motion. Note that this decomposition of motion is similar to that utilized in two-particle microrheology (23,24), only that we study the relative diffusion instead of correlations between particles.

The MSD of the parallel motion, $\langle \Delta r^2{}_{||} \rangle$ and the perpendicular motion, $\langle \Delta r^2{}_{\perp} \rangle$, are calculated using the standard time-averaged MSD definition,

$$\left\langle \Delta x^2(\tau) \right\rangle = \frac{\sum_{t=0}^{T-\tau} \left(x(t+\tau) - x(t)\right)^2}{T-\tau}, \qquad (1)$$

where T is the total measurement time, x is the coordinate, and τ is the averaging time window.

To extract the anomalous exponent from the MSD, one needs to take into account the effect of measurement errors. In our case of diffusion in the XY plane, our measurement noise produces a bias of $2\sigma^2{}_N = 5.2 \times 10^{-4}\ \mu\text{m}^2$ in parallel and perpendicular MSDs. When the population of diffusing particles is homogeneous, this bias can be treated though a subtraction from the ensemble-averaged MSD (25), and a simple fit to a power law. However, our trajectories come from a heterogeneous population and thus the mean logarithmic square displacement (MLSD) technique was implemented.

Mean logarithmic square displacement

Biological entities and particles moving in a biological media exhibit an inherent heterogeneity in the diffusion characteristics. This arises from differences in structure, bioactivity, local media composition, and more. In addition, limited sampling of a stochastic process increases the heterogeneity between measured trajectories. As a result of this heterogeneity, a population of anomalously diffusing particles, each obeying a time-averaged MSD of $\langle x_i^2 \rangle = D_i t^{\alpha_i}$, cannot be treated through ensemble averaging to extract the ensemble-averaged D or α, here designated $\langle D \rangle$ and $\langle \alpha \rangle$. In fact, a previous analysis (25) showed that the erroneous $\langle \alpha \rangle$ found in this way changes with time, and is strongly dependent on the distribution of α_i. At increasing time lags, higher α_i values dominate the ensemble average, leading to a transient anomalous diffusion.

To overcome this effect and enable the estimation of the ensemble average anomalous exponent, the mean logarithmic square displacement (MLSD) was proposed. For each particle, one calculates the logarithm of the square displacement:

$$\xi(\tau) = \log\left(\frac{\sum_{t=0}^{T-\tau} \left(x(t+\tau) - x(t)\right)^2}{T-\tau} \right), \qquad (2)$$

where τ and T are defined as in Eq. 1. Taking the ensemble average, or the MLSD, one finds the true average anomalous exponent:

$$\langle \xi(\tau) \rangle = \langle \log(D_i) \rangle + \langle \alpha \rangle \log(\tau). \qquad (3)$$

Measurement errors effect the MLSD similarly to the MSD, introducing a negative bias in the fit of the anomalous exponent. Here we subtracted $2\sigma^2{}_N$ from each individual trajectory and only then applied the logarithm and ensemble averaging. We fitted the MLSDs only for $\tau \geq 37$ s, where subtraction does not give negative values.

Note that possible differences between σ_N extracted from fixed cells and the measurement errors in live cells may leave a small residual bias in the MLSD. Such an increase in the measurement error would lead to the estimation of slightly lower anomalous exponents (25). However, this would not change the distance- and direction-dependent trends in $\langle \alpha \rangle$ that we find.

Quantile lines

Quantile lines are a common graphical representation of the cumulative distribution function (CDF) in time, which is handy when analyzing stochastic data. A full mathematical definition of quantile lines is given, for example, in Burnecki et al. (17). However, we also give a short description here for clarity.

A quantile line $P_i(t)$, with $i \leq 1$, is the value in time t for which $i \times 100\%$ of the data lies below. For example, the $P_{0.5}$, i.e., 50% quantile (hence median), of the series $Z(t) = \{1,4,5,8,10,3,9,7,6,2\}$ at time t is 5. For a stationary distribution (i.e., one that does not change in time), all quantile lines will remain constant with t. However, in experimental data, the limited amount of measurements does not allow the complete recreation of the CDF, and some fluctuation is expected.

Nuclear volume fluctuations

To observe monotonic expansions and contractions of the whole nucleus, we plotted the quantile lines of all nuclear distances for each cell. An expansion of the nucleus, for example, will cause all distances to increase, and show up in the quantile lines. However, because we are measuring the location of diffusing particles, it is expected that the quantile lines fluctuate in time.

To overcome this issue, we calculated confidence intervals for the 50, 75, and 90% quantiles, based on random sampling of trajectories from disjoint cells. For a cell with n tracked loci, we created 300 random sets of n loci that were randomly selected from different cells to form an artificial nucleus. Then the quantile lines of each of these artificial cells were calculated. Because loci were randomly chosen, any change in the quantiles is due to the random diffusion and not uniform volumetric changes or correlations between loci. The 95% confidence intervals for the 50, 75, and 95% quantiles were estimated from these random sets. Finally, the quantile lines of each measured cell were plotted and compared to the confidence intervals (see Fig. S1 and Section S1 in the Supporting Material).

Distribution of chromatin loci

To confirm the random distribution of chromatin loci in our measured nuclei, we simulated a random selection process of points from ellipsoids of varying sizes. For each ellipsoid, 100 sets of 400 pairs were chosen at random and normalized to the distance of the furthest pair. Then a histogram of all distances was compared to the normalized distance distribution of our measured loci. We then set a minimal distance cutoff at varying distances to simulate the minimal distance between chromatin loci pairs.

Comparing the histograms in Fig. S2, it is clear that a minimal distance condition is needed. Also, the best fitting was found for an ellipsoid of ratio 7:4:2 in the $X/Y/Z$ directions, respectively, where XY is the imaging plane and Z is parallel to the optical axis.

Stationarity of cellular dynamics

For each cell, we ran a series of tests to confirm stationarity of all trajectory increments throughout the measurement. For both the imaging plane coordinates XY and the relative coordinates ($r_{||,\perp}$), we plotted the actual increments (to observe large leaps) and quantile lines of the increments, for both single particle and the relative motion. Finally, we plotted the cumulative second moment, for each axis. If cells undergo periods of increased diffusion activity, we should observe it in the quantile lines as an expansion of the parallel lines, and a change of slope in the cumulative second moment.

All cells showed stationarity, except for the motion of centromeres in one cell, where several loci expressed increased motion over several time

points. This cell was taken out of the stochastic parameters analysis (see Figs. S3 and S4).

Gaussianity of increments

For each trajectory in each axis, we ran the Jarque-Bera, Lilliefors, and Anderson-Darling tests to confirm Gaussianity of the increments. The Jarque-Bera test checks whether the skewness and kurtosis of the sample match a Gaussian distribution. The Lilliefors test is an extension of the Kolmogorov-Smirnov test, and checks for normality when the variance and the mean of the Gaussian distribution are not specified, using the maximal distances between the CDF values of the sample and Gaussian distributions. Finally, the Anderson-Darling test is based on integration of quadratic distances between the CDFs of the sample and Gaussian distributions. The Anderson-Darling test is one of the most powerful tests to validate Gaussianity (26).

Rejection results for these tests at the $\alpha = 0.05$ level can be seen in Table 1. For a normal distribution (i.e., Gaussian increments), the rejection rates are expected to be ~5%, as it is in our case. Thus we conclude that both parallel and perpendicular relative motions have Gaussian increments.

Fractionally integrated moving averages analysis framework

A fractionally integrated moving average process, with memory parameter d and one moving average lag, is designated fractionally integrated moving averages (FIMA) (d,1) and represented by

$$(1 - B)^d X(t) = Z(t) - \psi Z(t - 1), \quad (4)$$

where $t = 0, \pm 1, \ldots$, B is the shift operator: $BX(t) = X(t-1)$, $-1/2 < d < 1/2$, which takes fractional values, either positive or negative, and $\{Z(t)\}$ is a white noise sequence (27–29). This is a general time-series construct adequate for modeling stochastic processes with a long-range autocovariance decaying by the power of $2d-1$ and an additional short-range, single time-step correlation between displacements.

In our case, we use the FIMA(d,1) framework to take into account both the long-range anomality of the diffusion process and the short-range effect of measurement error. This is based on the findings presented in Burnecki et al. (30). Measurement error is an uncorrelated process; however, when looking at its displacements, it shows a one time-point correlation function. Specifically, for a measurement error standard deviation of S, the incremental correlation function is $\rho(\Delta) = -S^2$ for $\Delta = 1$ and $\rho(\Delta) = 0$ for $\Delta > 1$. Thus, measurement error can be modeled by an MA(1) process. On the other hand, FBM has an infinite power-law decay of the incremental correlation function, similarly to $FI(d)$. In the limit of long trajectories, the anomalous exponent is equal to $2d-1$.

Thus, measurement error and an FBM process can be separated through the increment correlation function, as is done in our FIMA(d,1) estimation procedure. The parameter d is identified for each trajectory through a minimization of a functional as given in Burnecki and Sikora (31). Further technical details about the FIMA framework and its estimation are given in the Supporting Material.

TABLE 1 Percentage of trajectories for which we can reject a hypothesis (at the 5% significance level) that the increments follow the Gaussian law

	Centromeres			Telomeres		
	AD	JB	Li	AD	JB	Li
$\Delta r_{\|\|}$	5.3	7.2	4.9	5.6	8.0	5.3
$\Delta r_{\perp}$	5.1	7.8	5.2	6.0	8.5	5.5

AD, Anderson-Darling test; JB, Jarque-Bera test; Li, Lilliefors test.

Numerical simulations of nuclei

To validate our experimental results and models, we simulated diffusion of genetic loci in nuclei. Three-dimensional ellipsoids of the typical sizes in our systems were filled with 15–25 random particles, with a minimal distance of 1.5 μm between each pair. Then, each particle was given a random trajectory with the same typical diffusion characteristics as our experimental loci (i.e., $\alpha = 0.6$, $D = 4 \times 10^{-4}$ $\mu m^2/s^{0.6}$).

Afterwards, the ellipsoid was given a random rotation and drift motion, to simulate nucleus diffusion. We also incorporated the time delay in the sampling of different points, arising from the raster scan of the confocal system. The whole nucleus trajectory was simulated in finer detail than the individual loci. Then, based on the location of each locus in the three-dimensional volume, a time delay was attributed to it. The offset of the whole volume location was then subsampled for each loci based on its individual time delay. Finally, a Gaussian measurement error was added to each trajectory with the same standard deviation as our experimental system. (For more information, see Section C in the Supporting Material and Figs. S6 and S7.)

RESULTS

Fig. 1 *a* shows a typical U2OS nucleus cross section. Tracking telomeres and centromeres, and analyzing their time-averaged MSDs, showed that both loci perform anomalous diffusion. Fitting the average particle dynamics through the MLSD technique (25) gave a one-dimensional MSD of $\langle \Delta x^2(\tau) \rangle = 4 \times 10^{-4}\ \tau^{0.6}$ for telomeres and $\langle \Delta x^2(\tau) \rangle = 2.5 \times 10^{-4}\ \tau^{0.5}$ for centromeres.

Fig. 1 *b* shows the relative trajectories of several telomere pairs, from various cells, in the parallel and perpendicular coordinates. The relative trajectories taken from pairs at small $\bar{r} \approx 1.5$ μm show highly constrained motion. On the other hand, the trajectories from large $\bar{r} \approx 16$ μm show not only increased diffusion, but also differences between $\langle \Delta r^2_{||} \rangle$ and $\langle \Delta r^2_{\perp} \rangle$.

As a first step in the characterization of interloci motion, stationarity and Gaussianity were tested according to a previously published algorithm (17). The quantile test showed that internal chromatin diffusion is almost always stationary, except for in one cell, which was removed from analysis. Trajectory-wise analysis using the Jarque-Bera, Lilliefors, and Anderson-Darling tests proved that increment distribution is Gaussian.

In addition, for each nucleus, we tested whether the average distances between all loci are maintained in time, i.e., that the relative diffusion has zero mean. We found no significant monotonic expansions or contractions of interloci distances during our acquisition time.

Plotting the average MSD of all pairs against average pair distance, $\bar{r}$, and time, a clear trend appears for both telomeres and centromeres (Fig. 2). Relative diffusion is smaller in size at small interlocus distances, than at larger distances and interestingly, parallel and perpendicular motion strongly diverge at average pair distances $> \bar{r} = 7$ μm. While $\langle \Delta r^2_{\perp} \rangle$ converges toward the relative MSD of two independent particles, the $\langle \Delta r^2_{||} \rangle$ significantly increases with relative distance (for the MSD at a single time lag, see Fig. S5). Thus, a strong anisotropy is seen at large distances.

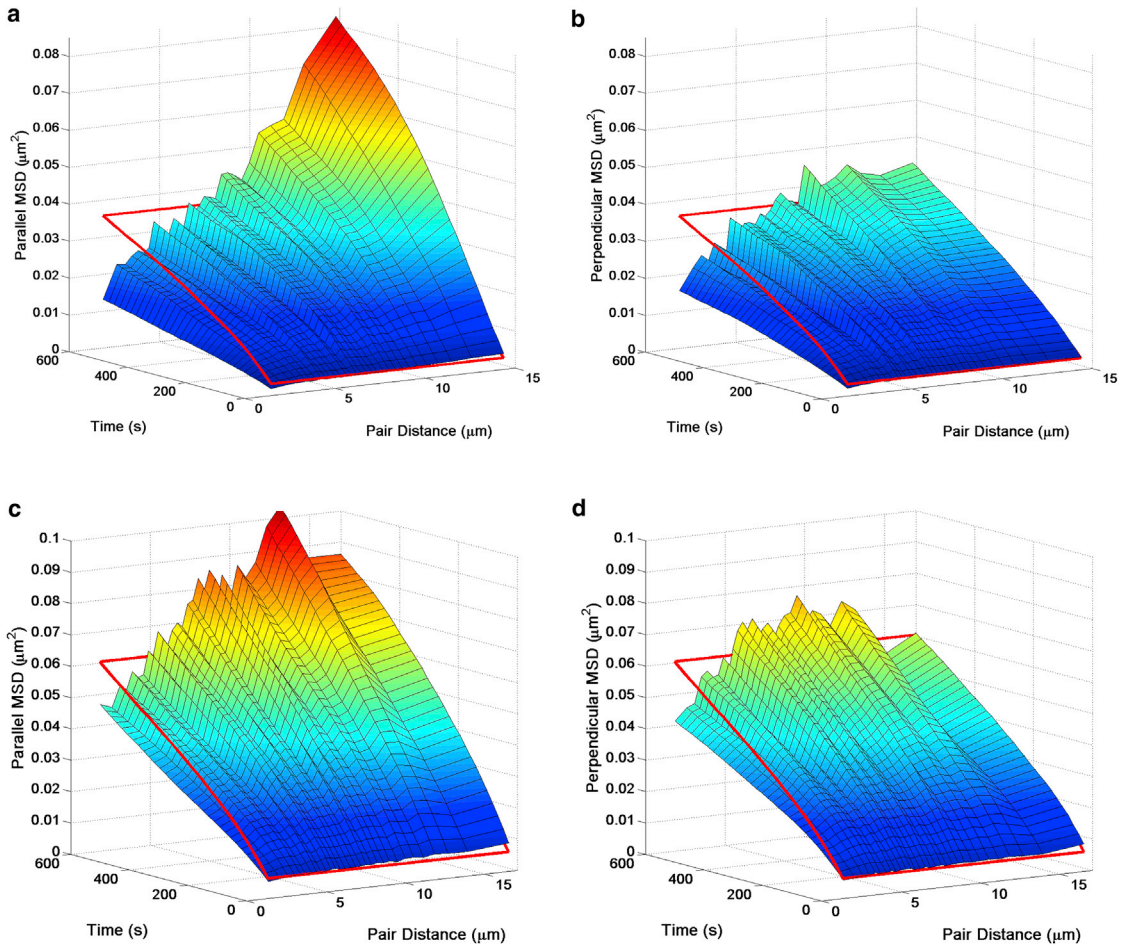

FIGURE 2 Average relative MSDs depend on distance and direction. The average $\langle \Delta r_{||}^2 \rangle$ (*a*) and $\langle \Delta r_{\perp}^2 \rangle$ (*b*) between centromeres depend on time and interlocus distance. (*Red line*) Expected diffusion for noninteracting loci pairs, equal to twice the average single locus MSD. Telomeres (*c* and *d*) show similar behavior. The relative diffusion is highly dependent on direction—$\langle \Delta_{||}^2 \rangle$ increases steadily with increasing distance, exceeding $\langle \Delta_{\perp}^2 \rangle$, which converges to a constant value. The results presented are after binning by distance into 30 equal sets, with 195 centromere and 347 telomere pairs per set. To see this figure in color, go online.

The parallel MSD at the largest distances is actually larger than that expected from independent particles with the chromatin diffusion characteristics. So, parallel relative motion is enhanced.

Next, we characterized the anomalous behavior of MSDs. Note that simple fitting of MSDs is prone to significant errors (25,32), leading us to use two separate techniques—MLSD and FIMA. MLSDs give the anomalous exponent of the average particle. Note also that the ensemble-averaged MSD has a strong temporal dependency on the heterogeneity of the population (Kepten et al. (25)), because particles with higher anomalous exponents become more dominant as the averaging window increases.

In addition, the FIMA framework was applied to directly measure the fractional memory of the process. FIMA is suitable in the analysis of stationary, time-correlated data, with an additional measurement error and no drift (Burnecki et al. (30,33); and see the Supporting Material). Specifically, the memory parameter d gives the fractional time dependency of the data, independently of other statistical properties. The MLSD technique gave us an accurate estimate of the anomalous dynamics, while the FIMA framework gave direct insight into the change in the fractional memory.

Similarly to the MSD size results (Fig. 2) the MLSD-extracted anomalous exponent shows distance dependence and anisotropy (Fig. 3 *a*). Starting at low values of $\alpha \sim 0.6$ in both axes, we observe a separation at distances of 7 μM. Notably, despite the qualitative similarity, telomere anomalous exponents are lower than centromere's exponents and their transition toward normality is slower. Because average dynamics have stationary and Gaussian increments, and a subdiffusive MSD, they can be characterized as FBM (17).

A similar distance dependency and anisotropy appear in the single trajectory d values retrieved from the FIMA framework (Fig. 3 *b*). The short-range similarity between axes and long-range separation is seen with strong resemblance to the behavior of average α-values. This strengthens

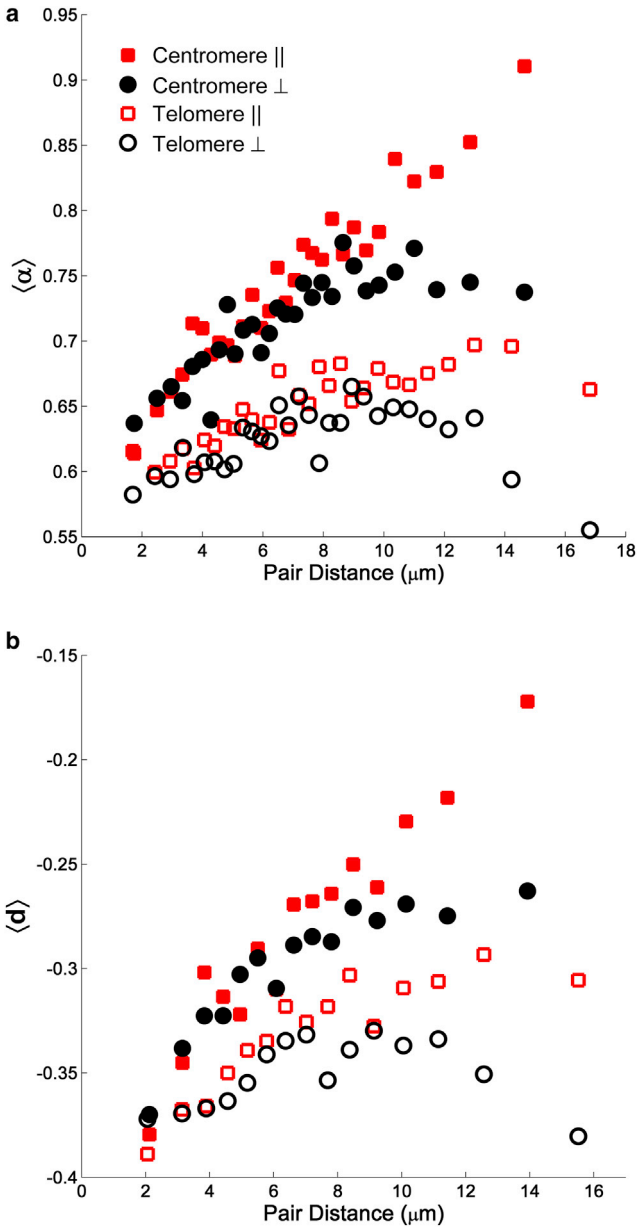

FIGURE 3 Fractional memory depends on distance and direction. (*a*) MLSD results of the average anomalous exponent for each average pair distance, $\bar{r}$. Centromere diffusion (*solid symbols*) is slightly less anomalous than telomere diffusion (*open symbols*). At small $\bar{r}$, parallel exponents (*black circles*) are similar to perpendicular exponents (*red squares*). As $\bar{r}$ increases, the two axes diverge. (*b*) Fractional memory FIMA d values are correlated with the anomalous exponent, presenting the same distance dependency and anisotropy. Binning as in Fig. 2, with FIMA results binned into 15 equal sets. To see this figure in color, go online.

our conclusion that interparticle motion is FBM with a distance-dependent anisotropic memory.

As a control, we also plotted the relative MSDs while taking loci pairs from a single focal plane. These gave the same trends, albeit with increased noise due to limited data. In addition, trajectories from fixed cells showed a constant, isotropic relative MSD with both time and distance.

Finally, we simulated loci diffusion in ellipsoids of the same dimensions as our typical nuclei. These simulations included both drift and rotation of the whole volume and an additional measurement error of the same magnitude as in our system. In addition, we included a time delay to the measurement of each locus based on the raster scanning performed in our confocal microscope. Such simulated systems did not show distance dependency of relative trajectories or their stochastic characteristics (Fig. S7, *a* and *b*).

DISCUSSION

A model for long-range dynamics

The enhancement of parallel motion with distance and the anisotropic nature of genetic loci diffusion have not been seen before, to the best of our knowledge. Models of relative particle motion in viscoelastic media predict that interparticle dynamics should be hindered at small distances and independent at long distances (23,24). Measurements and models of chromatin cross correlations at short times also did not identify this distance-dependent enhancement (21,34).

To explain the enhanced long-range parallel dynamics, we look for a model that is anisotropic, significant only at large distances and shifts toward motion that are normal and uncorrelated in time. The simplest such model is a series of expansions and contractions of the nuclear media. The parallel motion between two loci is enhanced by the total expansion or contraction of the interconnected media between them. The perpendicular motion is not affected by dilation and thus converges to the independent interparticle MSD. A more-detailed discussion of expansion and contraction dynamics, as well as related models, can be found in the Supporting Material.

We take two particles at distance r and expand or contract the media between them by a factor $l > 0$, so that the new distance between the pair is lr. The total expansion at time t, $L(t)$, after a series of $n = 1/\tau$ subsequent fluctuations is the product of all n individual fluctuations (where we have assumed fluctuations occur every τ). Taking n to be large, the central limit theorem can be applied giving $L(t) \sim \mathrm{Log}N(\mu,\sigma)$, with $\mathrm{Log}N(\mu,\sigma)$ designating a log-normal distribution.

We have seen that the average distances between loci are maintained in time, hence the geometric mean of $L(t)$ is 1 and $\mu = 0$. Now we look at the MSD between two particles at average distance $\bar{r}$ and assume that the fluctuations around $\bar{r}$ are small, $\Delta r \ll \bar{r}$. This implies that the parallel MSD $\langle \Delta r_{\parallel}^2 \rangle = \bar{r}^2 \langle L(t)^2 \rangle$. Thus, the MSD between two particles increases with the square of the distance.

For a log-normal distribution, $\mathrm{Var}[\mathrm{Log}N(\mu,\sigma)] = e^{2\mu+\sigma^2}(e^{\sigma^2}-1)$. Expanding the exponents, we find $\langle L(t) \rangle \approx \sigma(t)^2$. Using the central limit theorem for $\tilde{L} = \log(L(t))$, after n subsequent steps, $\mathrm{Var}[\tilde{L}] = n\sigma^2$. Defining $D_U = \sigma^2/\tau$ and taking $\tau, \sigma \to 0$, we find that $\mathrm{Var}[\tilde{L}] = D_U t$ (remember that

$n = t/\tau$). Summing up our derivation, we find that the parallel diffusion between two particles at average distance $\overline{r}$ obeys

$$\left\langle \Delta r_{\parallel}^{2} \right\rangle \approx \overline{r}^{2} D_U t. \quad (5)$$

We name D_U, which has units of [1/s], the uniform contraction-expansion (UCE) diffusion coefficient. Note that this relation holds only at the limit of small σ. At long times, we expect that cellular constraints prevent further expansion and contraction of the media, and that the linearity in time diminish. Note that UCE diffusion is normal, has no memory, and is anisotropic—thus matching all our findings.

Fitting the relative parallel MSD for distances where the relative motion is higher than the independent MSD (where the hindering correlations have decayed), we can extract $D_U t$ for various times (Fig. 4, *a* and *b*). Then, we fit the results to find D_U for both centromere and telomere populations (Fig. 4 *c*). For centromeres, we find a UCE coefficient of $D_U = 5.3 \times 10^{-7}$ s^{-1}, while for telomeres, $D_U = 3.6 \times 10^{-7}$ s^{-1}. Interestingly, at long times of $t > 450$ s there is a decrease in the fitted $D_U t$ value, perhaps indicating a limit to the magnitude of dilations for telomeres and centromeres.

UCE diffusion not only fits the stochastic characteristics of the diffusion, but also the spatiotemporal functional form. Other models, such as random local expansions ($\langle r^2{}_{||} \rangle$ is linear with $\overline{r}$) or transport of loci (quadratic in t), would not adequately fit the data.

Returning to our simulated nuclei, we incorporated UCE diffusion into our simulations. This completely recreated the long-range anisotropy seen in our measured cells (Fig. S7). We remind that in our null hypothesis simulations (without the UCE diffusion mechanism), no long-range effects were seen.

Using the fitted coefficients of D_U for telomeres and centromeres, we can estimate the magnitude of the contractile dynamics. We find that in 1 min, relative motion between two loci at a distance of 10 μm will be on a scale of 46–56 nm for telomeres and centromeres, respectively. These motions are of subpixel magnitude, and cannot be seen by standard fluorescent microscopy (Movies S1 and S2). Together with the negligible magnitude of fluctuations in the short time domains, this is perhaps why D_U has not been characterized before.

Site-dependent coupling

The general attributes of telomere and centromere motion are similar and fit the contractile motion proposed. However, several differences can be seen between telomeres and centromeres, enabling us to look into variances between different chromosomal loci. Centromeres show higher relative anomalous exponents and memory parameters at all distances. In addition, their D_U is higher by $\approx 50\%$, while their single particle dynamics are slower.

A possible explanation to these differences lays in the stronger interaction that centromeres have with the rest of the chromatin chain. Telomeres that are the end segments of the chromosomes can diffuse more freely compared to centromeres, while centromeres are more highly coupled to long-range chromatin motions such as uniform expansions and contractions. This coupling leads to higher D_U, which, due to the slower independent dynamics, becomes more significant in shorter scales and time spans. As derived above, the contractile mechanism leads to higher anomalous exponents and memory parameters, fitting the results of relative centromere dynamics.

Biological implications

Telomeres and centromeres showed constrained relative dynamics at short distances of a few micrometers. This

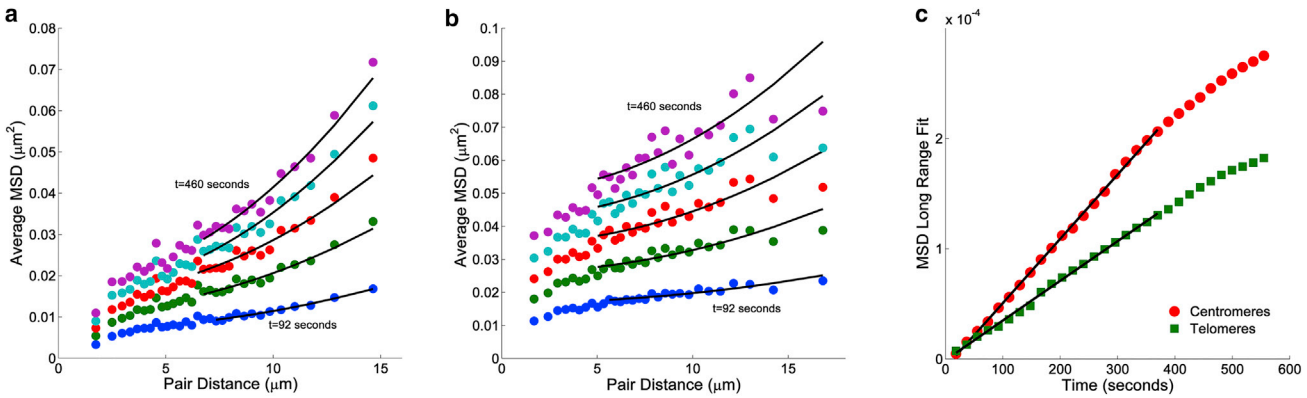

FIGURE 4 Estimation of the UCE diffusion coefficient. (*a*) The relative parallel MSD of centromeres (*colored circles*) is fitted to a quadratic curve for various times at distances where the relative MSD is higher than the independent MSD (*black lines*). Here we show results for 92, 184, 277, 370, and 460 seconds. Note that we use $\langle \Delta r_{||}^{2} \rangle = a\overline{r}^{2} + b$ form with no linear term. (*b*) Same as (*a*) but for telomeres. (*c*) The extracted *a* values are fitted to a straight line to give the UCE diffusion coefficient, D_U. A decrease in relative diffusion can be seen at long times, possibly due to confinement, leading us to omit them from the fit. Telomere long-distance fits (*green squares*) are not as good as for centromeres (*red circles*), but still gave linear temporal dependency of the UCE diffusion. To see this figure in color, go online.

constraining has been observed previously for shorter timescales in both human cells and yeast (21,35). In Bruinsma et al. (34), a viscoelastic model was proposed, which gives rise to the constraining across several microns (and chromosome territories) found in Zidovska et al. (21). Here we have found that these correlations propagate to much longer times, at least 30 min. Interestingly, despite the different nature of telomeres and centromeres, they showed similar constraining and relative motion. This strengthens the suggested viscoelastic model, which is not dependent on site-specific interactions.

We suggest that the short-range constraining of relative motion serves to prevent the loss of chromosomal folding due to the continuous diffusion. If genetic sites were allowed to diffuse without correlation to their neighbors, spatial relations and folding motifs would deteriorate with time. Because loci that are close to each other tend to show reduced relative diffusion, their relative spatial positions are preserved over longer times. We leave the prediction of structural decoherence times and their dependency on various diffusion parameters for future work.

As mentioned above, particles moving in an equilibrium viscoelastic media are expected to become independent with growing distance. However, the UCE dynamics increase with distance and thus present a unique biophysical process. It is, as of this writing, unclear what the source may be for the UCE diffusion. One possibility is that the required forces for uniform nuclear deformation originate from the anchoring of the cytoskeleton to the nuclear lamina and from there to the chromatin strands (36,37). In such a model, the continuous building of the cytoskeleton due to cell migration and deformation, exerts fluctuating forces on the nucleus. The nucleus reacts as a damper to these forces, elastically stretching or compressing.

Various studies have given a typical nuclear rigidity of 5 kPa (38–40). The tensional modulus and compression model are dependent on the way the nucleus is perturbed (41). However, here we are dealing with small deformations, enabling us to use the classical Young modulus, E_Y, and the Hookean deformation regime. In this model, a solid with cross-section A_0 and length L_0, under tensional force F, will undergo an elastic deformation of $\Delta r = E_Y A_0 F / L_0$. For the in-plane deformations in our system, this gives a force of

$$F = \pi E_Y h \Delta r, \tag{6}$$

where we have used a cross section of an ellipse orthogonal to the imaging plane, and h is the thickness of the nucleus.

Using a typical $\Delta r \approx 50$ nm in the minute time regime, and $h \approx 4.5$ nm, Eq. 6 gives $F \approx 3.5$ nN. Such forces are in the regime of other nuclear deformation processes (42). Note that if plastic deformation is also taking place in the nucleus, the effective modulus will be lower, and the forces needed will also be lower. Thus, it appears that UCE diffusion in the nucleus may indeed arise from extranuclear forces. Further studies in cells with softer nuclei or disturbed cytoskeleton structure may help illuminate the origin of the UCE dynamics.

Previous studies (43) have seen localized dilation dynamics of chromatin domains in embryonic stem (ES) cells. Because Talwar et al. (43) observed that ATP depletion significantly lowered expansion dynamics, we also attempted to measure interloci dynamics in these conditions. However, differentiated cell chromatin diffuses slower than in ES cells. The further reduction in diffusion after ATP depletion prevented the accurate characterization of expansions and contractions in our U2OS cells. It would be interesting to measure relative dynamics in ES, and observe whether they too show UCE diffusion.

Extending our results for telomeres and centromeres to general chromatin diffusion, we suggest that cells adopt an optimal combination of nuclear diffusion modes. While short-range dynamics are constrained, and thus retain organization, long-range dynamics react to external forces and stresses. Thus the nucleus remains organized while enabling a structural deformation with changing cellular conditions.

Our stochastic methodology can also be extended to common physical systems described with Lévy stable distributions that have found broad applications (44,45). UCE diffusion can be classified as a transient subordinated anomalous diffusion (46). Finally, UCE diffusion serves as a basis for future studies of dynamic systems. Our multiple tracer technique enables its measurement even where previously unseen by other imaging techniques—leading to the expectation that UCE diffusion will be identified in various physical and biological systems.

SUPPORTING MATERIAL

Supporting graphs, additional theoretical background, analysis results for single cells, and two movies are available at http://www.biophysj.org/biophysj/supplemental/S0006-3495(15)00766-3.

AUTHOR CONTRIBUTIONS

E.K. designed the project and performed experiments, and analyzed and modeled data; I.B. designed and performed experiments; A.W. and K.B. analyzed and modeled data; Y.G. designed the project and modeled data; and all authors wrote the article.

ACKNOWLEDGMENTS

E.K., I.B., and Y.G. were supported in part by the Israel Centers of Research Excellence No. 1902/12, and Israel Science Foundation grant No. 51/12. K.B. and A.W. were supported by the National Science Center Maestro Grant No. 2012/06/A/ST1/00258.

REFERENCES

1. Spector, D. L. 2003. The dynamics of chromosome organization and gene regulation. *Annu. Rev. Biochem.* 72:573–608.

2. Gilbert, N., S. Gilchrist, and W. A. Bickmore. 2005. Chromatin organization in the mammalian nucleus. *Int. Rev. Cytol.* 242:283–336.
3. Misteli, T. 2007. Beyond the sequence: cellular organization of genome function. *Cell.* 128:787–800.
4. Heard, E., and W. Bickmore. 2007. The ins and outs of gene regulation and chromosome territory organisation. *Curr. Opin. Cell Biol.* 19: 311–316.
5. Mirny, L. A. 2011. The fractal globule as a model of chromatin architecture in the cell. *Chromosome Res.* 19:37–51.
6. Dostie, J., and W. A. Bickmore. 2012. Chromosome organization in the nucleus—charting new territory across the Hi-Cs. *Curr. Opin. Genet. Dev.* 22:125–131.
7. de Wit, E., and W. de Laat. 2012. A decade of 3C technologies: insights into nuclear organization. *Genes Dev.* 26:11–24.
8. Barkai, E., Y. Garini, and R. Metzler. 2012. Strange kinetics of single molecules in living cells. *Phys. Today.* 65:29–35.
9. Mason, T., K. Ganesan, …, S. Kuo. 1997. Particle tracking microrheology of complex fluids. *Phys. Rev. Lett.* 79:3282.
10. Abney, J. R., B. Cutler, …, B. A. Scalettar. 1997. Chromatin dynamics in interphase nuclei and its implications for nuclear structure. *J. Cell Biol.* 137:1459–1468.
11. Vazquez, J., A. S. Belmont, and J. W. Sedat. 2001. Multiple regimes of constrained chromosome motion are regulated in the interphase *Drosophila* nucleus. *Curr. Biol.* 11:1227–1239.
12. Molenaar, C., K. Wiesmeijer, …, R. W. Dirks. 2003. Visualizing telomere dynamics in living mammalian cells using PNA probes. *EMBO J.* 22:6631–6641.
13. Levi, V., Q. Ruan, …, E. Gratton. 2005. Chromatin dynamics in interphase cells revealed by tracking in a two-photon excitation microscope. *Biophys. J.* 89:4275–4285.
14. Jegou, T., I. Chung, …, K. Rippe. 2009. Dynamics of telomeres and promyelocytic leukemia nuclear bodies in a telomerase-negative human cell line. *Mol. Biol. Cell.* 20:2070–2082.
15. Bronstein, I., Y. Israel, …, Y. Garini. 2009. Transient anomalous diffusion of telomeres in the nucleus of mammalian cells. *Phys. Rev. Lett.* 103:018102.
16. Metzler, R., and J. Klafter. 2000. The random walk's guide to anomalous diffusion: a fractional dynamics approach. *Phys. Rep.* 339:1–77.
17. Burnecki, K., E. Kepten, …, A. Weron. 2012. Universal algorithm for identification of fractional Brownian motion. A case of telomere subdiffusion. *Biophys. J.* 103:1839–1847.
18. Rosa, A., and R. Everaers. 2008. Structure and dynamics of interphase chromosomes. *PLOS Comput. Biol.* 4:e1000153.
19. Fritsch, C. C., and J. Langowski. 2011. Chromosome dynamics, molecular crowding, and diffusion in the interphase cell nucleus: a Monte Carlo lattice simulation study. *Chromosome Res.* 19:63–81.
20. Soutoglou, E., and T. Misteli. 2007. Mobility and immobility of chromatin in transcription and genome stability. *Curr. Opin. Genet. Dev.* 17:435–442.
21. Zidovska, A., D. A. Weitz, and T. J. Mitchison. 2013. Micron-scale coherence in interphase chromatin dynamics. *Proc. Natl. Acad. Sci. USA.* 110:15555–15560.
22. Kepten, E., A. Weron, …, Y. Garini. 2015. Guidelines for the fitting of anomalous diffusion mean square displacement graphs from single particle tracking experiments. *PLoS One.* 10:e0117722.
23. Crocker, J. C., M. T. Valentine, …, D. A. Weitz. 2000. Two-point microrheology of inhomogeneous soft materials. *Phys. Rev. Lett.* 85: 888–891.
24. Crocker, J. C., and B. D. Hoffman. 2007. Multiple-particle tracking and two-point microrheology in cells. *Methods Cell Biol.* 83:141–178.
25. Kepten, E., I. Bronshtein, and Y. Garini. 2013. Improved estimation of anomalous diffusion exponents in single-particle tracking experiments. *Phys. Rev. E Stat. Nonlin. Soft Matter Phys.* 87:052713.
26. Stephens, M. A. 1974. EDF statistics for goodness of fit and some comparisons. *J. Am. Stat. Assoc.* 69:730–737.
27. Parada, L. M., and X. Liang. 2004. Optimal multiscale Kalman filter for assimilation of near-surface soil moisture into land surface models. *J. Geophys. Res. Atmosph.* 109:1984–2012.
28. Brockwell, P. J. 2002. Introduction to Time Series and Forecasting, Vol. 1. Taylor & Francis, New York.
29. Brockwell, P. J., and R. A. Davis. 1994. ITSM for Windows: A User's Guide to Time Series Modeling and Forecasting/Book and Disk. Springer Science & Business Media, New York.
30. Burnecki, K., E. Kepten, …, A. Weron. 2015. Estimating the anomalous diffusion exponent for single particle tracking data with measurement errors—an alternative approach. *Sci. Rep.* 5:11306.
31. Burnecki, K., and G. Sikora. 2013. Estimation of FARIMA parameters in the case of negative memory and stable noise. *IEEE Trans. Signal Process.* 61:2825–2835.
32. Vestergaard, C. L., P. C. Blainey, and H. Flyvbjerg. 2014. Optimal estimation of diffusion coefficients from single-particle trajectories. *Phys. Rev. E Stat. Nonlin. Soft Matter Phys.* 89:022726.
33. Burnecki, K., G. Sikora, and A. Weron. 2012. Fractional process as a unified model for subdiffusive dynamics in experimental data. *Phys. Rev. E Stat. Nonlin. Soft Matter Phys.* 86:041912.
34. Bruinsma, R., A. Y. Grosberg, …, A. Zidovska. 2014. Chromatin hydrodynamics. *Biophys. J.* 106:1871–1881.
35. Backlund, M. P., R. Joyner, …, W. E. Moerner. 2014. Correlations of three-dimensional motion of chromosomal loci in yeast revealed by the double-helix point spread function microscope. *Mol. Biol. Cell.* 25:3619–3629.
36. Mammoto, A., T. Mammoto, and D. E. Ingber. 2012. Mechanosensitive mechanisms in transcriptional regulation. *J. Cell Sci.* 125:3061–3073.
37. Houben, F., F. Ramaekers, …, J. Broers. 2007. Role of nuclear lamina-cytoskeleton interactions in the maintenance of cellular strength. *Biochim. Biophys. Acta.* 1773:675–686.
38. Azeloglu, E. U., J. Bhattacharya, and K. D. Costa. 2008. Atomic force microscope elastography reveals phenotypic differences in alveolar cell stiffness. *J. Appl. Physiol.* 105:652–661.
39. Caille, N., O. Thoumine, …, J.-J. Meister. 2002. Contribution of the nucleus to the mechanical properties of endothelial cells. *J. Biomech.* 35:177–187.
40. Krause, M., J. Te Riet, and K. Wolf. 2013. Probing the compressibility of tumor cell nuclei by combined atomic force-confocal microscopy. *Phys. Biol.* 10:065002.
41. Chen, J. 2014. Nanobiomechanics of living cells: a review. *Interface Focus.* 4:20130055.
42. Revach, O.-Y., A. Weiner, …, B. Geiger. 2015. Mechanical interplay between invadopodia and the nucleus in cultured cancer cells. *Sci. Rep.* 5:9466.
43. Talwar, S., A. Kumar, …, G. V. Shivashankar. 2013. Correlated spatiotemporal fluctuations in chromatin compaction states characterize stem cells. *Biophys. J.* 104:553–564.
44. Weron, A., and M. Magdziarz. 2010. Generalization of the Khinchin theorem to Lévy flights. *Phys. Rev. Lett.* 105:260603.
45. Dechant, A., E. Lutz, …, E. Barkai. 2011. Fluctuations of time averages for Langevin dynamics in a binding force field. *Phys. Rev. Lett.* 107:240603.
46. Stanislavsky, A., K. Weron, and A. Weron. 2014. Anomalous diffusion with transient subordinators: a link to compound relaxation laws. *J. Chem. Phys.* 140:054113.